B1359+154: A Six Image Lens Produced by a z≃1 Compact Group of Galaxies[1]

D. Rusin[2], C.S. Kochanek[3], M. Norbury[4]

E.E. Falco[3], C.D. Impey[5], J. Lehár[3], B.A. McLeod[3]

H.-W. Rix[6], C.R. Keeton[5], J.A. Muñoz[7], C.Y. Peng[5]

ABSTRACT

HST V and I-band observations show that the gravitational lens B1359+154 consists of six images of a *single* $z_s = 3.235$ radio source and its star-forming host galaxy, produced by a compact group of galaxies at $z_l \simeq 1$. VLBA observations at 1.7 GHz strongly support this conclusion, showing six compact cores with similar low-frequency radio spectra. B1359+154 is the first example of galaxy-scale gravitational lensing in which more than four images are observed of the same background source. The configuration is due to the unique lensing mass distribution: three primary lens galaxies lying on the vertices of a triangle separated by $0\farcs7 \simeq 4h^{-1}$ kpc, inside the $1\farcs7$ diameter Einstein ring defined by the radio images. The gravitational potential has additional extrema within this triangle, creating a pair of central images that supplement the "standard" four-image geometry of the outer components. Simple mass models consisting of three lens galaxies constrained by HST and VLBA astrometry naturally reproduce the observed image positions but must be finely-tuned to fit the flux densities.

Subject headings: cosmology: gravitational lensing; galaxy groups

---

[1]Based on observations made with the NASA/ESA Hubble Space Telescope, obtained at the Space Telescope Science Institute, which is operated by AURA, Inc., under NASA contract NAS 5-26555.

[2]Department of Physics and Astronomy, University of Pennsylvania, 209 S. 33rd St., Philadelphia, PA 19104-6396 (email:drusin@hep.upenn.edu)

[3]Harvard-Smithsonian Center for Astrophysics, 60 Garden St., Cambridge, MA 02138 (email: ckochanek, efalco, jlehar, bmcleod@cfa.harvard.edu)

[4]Jodrell Bank Observatory, University of Manchester, Macclesfield, Cheshire SK11 9DL, UK (email: mn@jb.man.ac.uk)

[5]Steward Observatory, University of Arizona, Tucson, AZ 85721 (email: impey, ckeeton, cyp@as.arizona.edu)

[6]Max-Planck-Institut fuer Astronomie, Koenigsstuhl 17, D-69117 Heidelberg, Germany (email: rix@mpia-hd.mpg.de)

[7]Instituto de Astrofisica de Canarias, Via Lactea, E38200 La Laguna, Tenerife, Spain (email: jmunoz@ll.iac.es)

1. Introduction

The vast majority of the ~ 60 known arcsecond-scale gravitational lens systems consist of two or four detectable images, consistent with the generic lensing properties of smooth, isolated and centrally steep mass distributions (e.g. Blandford & Kochanek 1987). There are very few cases in which a "non-standard" number of images may have been observed.[8] APM08279+5255 (Ibata et al. 1999) and MG1131+0456 (Chen & Hewitt 1993) each contain a central component that could be an additional lensed image created by a sufficiently large galaxy core or shallow mass profile (Narasimha, Subramanian & Chitre 1986; Rusin & Ma 2000). Alternatively, APM08279+5255 may be a special class of imaging produced by an edge-on disk (Keeton & Kochanek 1998), while the central component in MG1131+0456 could be weak AGN emission associated with the lensing galaxy. In addition, MG2016+112 (Lawrence et al. 1984; Garrett et al. 1996) exhibits a rather complicated image morphology consisting of four primary components, one of which has three subcomponents in VLBI maps. This may be a compound lens produced by two galaxies at different redshifts (Nair & Garrett 1997). Benitez et al. (1999) suggest an alternative model, but it might not fully explain the VLBI observations.

Complex interplay between mass distributions can lead to lens systems with more than four images of a source. For example, ellipsoidal mass distributions perturbed by shear fields may produce configurations with six or eight images arranged about the tangential critical curve (Keeton, Mao & Witt 2000b). However, this requires that the relative magnitudes and orientations of the internal and external shear axes be finely tuned, and the resulting cross-sections are quite small. Compound mass distributions have been shown to be far more efficient at producing a variety of complex geometries in which five or more images may be formed over a range of radii (Kochanek & Apostolakis 1988). This has been observed in the cluster-lensing case, where substructure in the gravitational potential created by the resident galaxies can qualitatively alter the lensing properties that one would expect for a smooth halo mass distribution (e.g. Natarajan et al. 1998; Meneghetti et al. 2000). A dramatic example of this is CL0024+1654, which exhibits eight images of a single blue background galaxy (Kassiola, Kovner & Fort 1992; Wallington, Kochanek & Koo 1995; Colley, Tyson & Turner 1996; Tyson, Kochanski & Dell'Antonio 1998).

Early-type galaxies preferentially participate in lensing (Kochanek et al. 2000a), so a large fraction of lens galaxies should be members of small groups and clusters due to the morphology-density relation (Dressler 1980; see also Keeton, Christlein & Zabludoff 2000a). Indeed, many lens systems are known to be perturbed by nearby galaxies (e.g. B2319+051; Rusin et al. 2000b), groups (e.g. PG1115+080; Schechter et al. 1997), or clusters (e.g. QSO 0957+561, Fischer et al. 1997; RXJ0921+4529, Muñoz et al. 2000). A handful of systems are lensed by more than one primary galaxy (e.g. B1127+385, Koopmans et al. 1999; B1608+656, Koopmans

[8] B1933+503 (Sykes et al. 1998) and B1938+666 (King et al. 1997) contain ten and six lensed radio components, respectively, but this is due to the imaging of a multi-component source rather than any exotic properties of the lensing potential.

& Fassnacht 1999), but in these cases standard image geometries are produced despite merged caustics. Several additional lenses are observed to have faint satellite galaxies as companions inside or near the Einstein radius (e.g. MG0414+0534, Schechter & Moore 1993; B1030+074, Xanthopoulos et al. 1998; B1152+199, Rusin et al. in preparation). While the likelihood of finding nearly equal mass galaxies close enough to have merged caustics is predicted to be only $\sim 1\%$ (Kochanek & Apostolakis 1988), the probability of finding fainter satellites near the primary lens is not small because galaxy luminosity functions diverge for faint galaxies – all lenses should have faint neighbors, as discussed in the Appendix. While such systems typically produce regions of the source plane in which more than four images can form, the small size of the companion galaxies means that the cross-sections for creating non-standard image geometries are not significant.

The gravitational lens system B1359+154 (Myers et al. 1999), discovered in the Cosmic Lens All-Sky Survey (CLASS; e.g. Myers et al. 1995), has been suspected of containing more than four lensed images. Observations with the Very Large Array (VLA) and Multi-Element Radio-Linked Interferometer Network (MERLIN) show a total of six radio components (Myers et al. 1999; Rusin et al. 2000a). Four of these components (A–D) are arranged in a typical quad-lens configuration (maximum image separation of $1\farcs7$), with two additional components (E and F) residing within the ring defined by the outer images. Preliminary radio spectral studies of B1359+154 at high frequency (Myers et al. 1999) suggested that E had a slightly flatter spectrum than A–D, and therefore that the central components may be core-jet emission associated with a weak AGN in the lensing galaxy or galaxies, as in the case of B2045+265 (Fassnacht et al. 1999). When the spectra were extended down to 5 GHz, however, there appeared to be less disparity among the radio components (Rusin et al. 2000a). Subsequent VLA observations at 15 GHz have failed to decisively confirm that E is flatter than A–D at high-frequency, or detect component F. Spectroscopy with the Keck II telescope determined the source redshift to be $z_s = 3.235$ (Myers et al. 1999). Adaptive optics observations of B1359+154 conducted with the Canada-France Hawaii Telescope (CFHT) in the infrared K$'$ band (Rusin et al. 2000a) detected counterparts to radio components A–D, and discovered three extended emission peaks (K1–K3) bracketing the expected positions of E and F. K1–K3 were identified as three possible lensing galaxies, comprising the core of a compact galaxy group. Evidence of an arc connecting A, B and C was also observed, along with a weaker emission feature associated with component E. The compound deflector system not only explained why attempts to model the outer four components using a single galaxy had failed (Myers et al. 1999), but offered the means of creating additional extrema in the lensing potential. This opened the possibility that at least one of the central components is a lensed image.

In this paper we present powerful new evidence from observations with the Hubble Space Telescope (HST) and Very Long Baseline Array (VLBA) that B1359+154 consists of six images of a *single* background source, lensed by a compact group of galaxies at $z_l \simeq 1$. In §2 we present VLBA observations of B1359+154 and investigate the low-frequency radio spectra of the components. In §3 we discuss and analyze HST V and I-band observations, which offer compelling evidence for the six-image hypothesis. In §4 we use preliminary mass modeling to demonstrate that

B1359+154 can be naturally explained as a true six-image lens system. Finally, in §5 we discuss the prospects for obtaining improved constraints on the lensing mass distribution of B1359+154, and ultimately using the system to study the structure of small galaxy groups at high redshift.

2. VLBA Imaging of B1359+154

VLBA observations of B1359+154 were obtained at 1.7 GHz on 1999 December 10 for an on-source integration time of 2 hr, and again on 2000 Aug 28 for 8 hr. These observations were performed by iterating between the target source for 3 min and the nearby phase-reference calibrator B1413+150 for 1.5 min. The data for each of the two epochs were calibrated separately within the AIPS data reduction package, then mapped and model-fit using DIFMAP. The flux densities of the model-fit components exhibited little variation ($\sim 3\%$) between epochs, so the two data sets were combined to improve the signal-to-noise. The resulting naturally-weighted map of B1359+154 is presented in Fig. 1, and has an rms noise level of 45 μJy/beam. All six radio components seen in previous VLA and MERLIN observations are easily detected by the VLBA, and maps of the individual components are shown in Fig. 2. Components A, B, and C each exhibit a compact core with associated jet emission. Lensing-induced parity reversal is evident in the relative orientations of the subcomponents. Components D, E and F are each unresolved. The data were modeled within DIFMAP using a total of 9 gaussian components (Table 1): 6 compact cores (A1–F1), 1 extended jet (A2) and 2 compact subcomponents (B2, C2).

The compact nature of radio components E and F strongly argue for their identification as additional lensed images, rather than weak core-jet emission associated with the lensing mass (Myers et al. 1999). First, it would be rare for jet emission to remain unresolved at ~ 10 mas resolution. All but one pair of radio components shown to be similarly compact in CLASS VLBA follow-up observations is a pair of lensed images, the only exception being the binary quasar B0827+525 (Koopmans et al. 2000). There is also no evidence in the VLBA data to suggest that any emission bridge might be connecting E and F. Second, it is unlikely that both E and F could mark the cores of independent AGN within the deflector. One would expect the positions of AGN to be correlated with brightness peaks of the lensing galaxies, and this is not the case in the CFHT data. Third, the structure of all six radio components are morphologically consistent with a single background source. Specifically, if the source consists of a core and weak jet, it is likely that extended emission would be visible in the more magnified lensed images while the fainter images show only the compact core. This is exactly what is observed in B1359+154: A–C are bright and exhibit weak subcomponents; D–F are faint and share identical unresolved morphologies.

Next we construct low-frequency radio spectra of the components by combining the 1.7 GHz VLBA flux densities with those previously obtained at 5 GHz using MERLIN (Rusin et al. 2000a) and at 8.5 GHz using the VLA (Myers et al. 1999). One need not be concerned about combining data from different epochs as there is little evidence for any significant variability in the lensed source. The resulting radio spectra are plotted in Fig. 3 and exhibit striking similarities. Each of

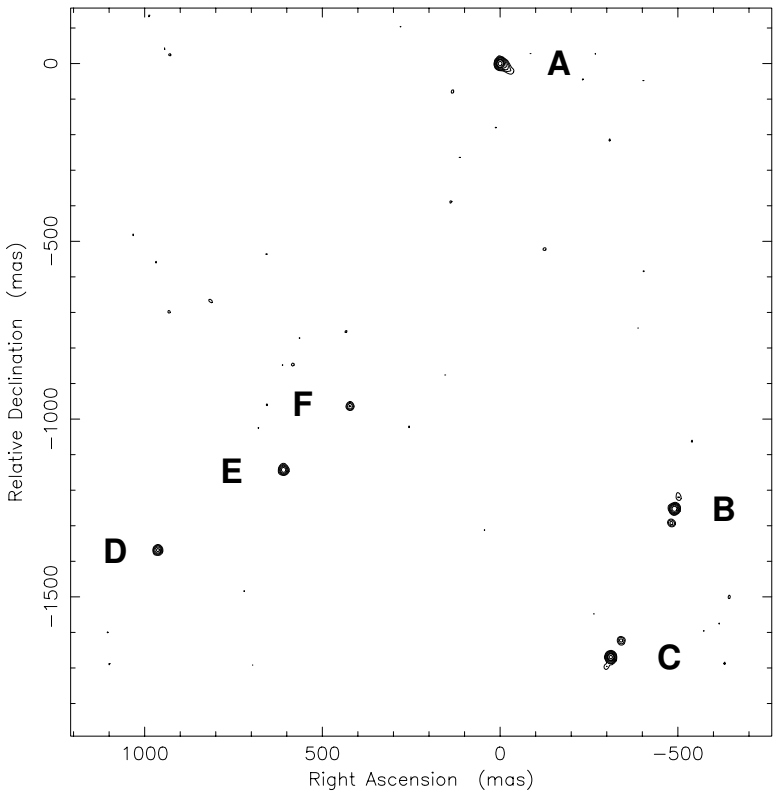

Fig. 1.— VLBA 1.7 GHz naturally-weighted map of B1359+154. The data is restored with a beam of size 13.9×12.5 mas at PA $= -3.34°$. The map rms noise level is 45 μJy/beam.

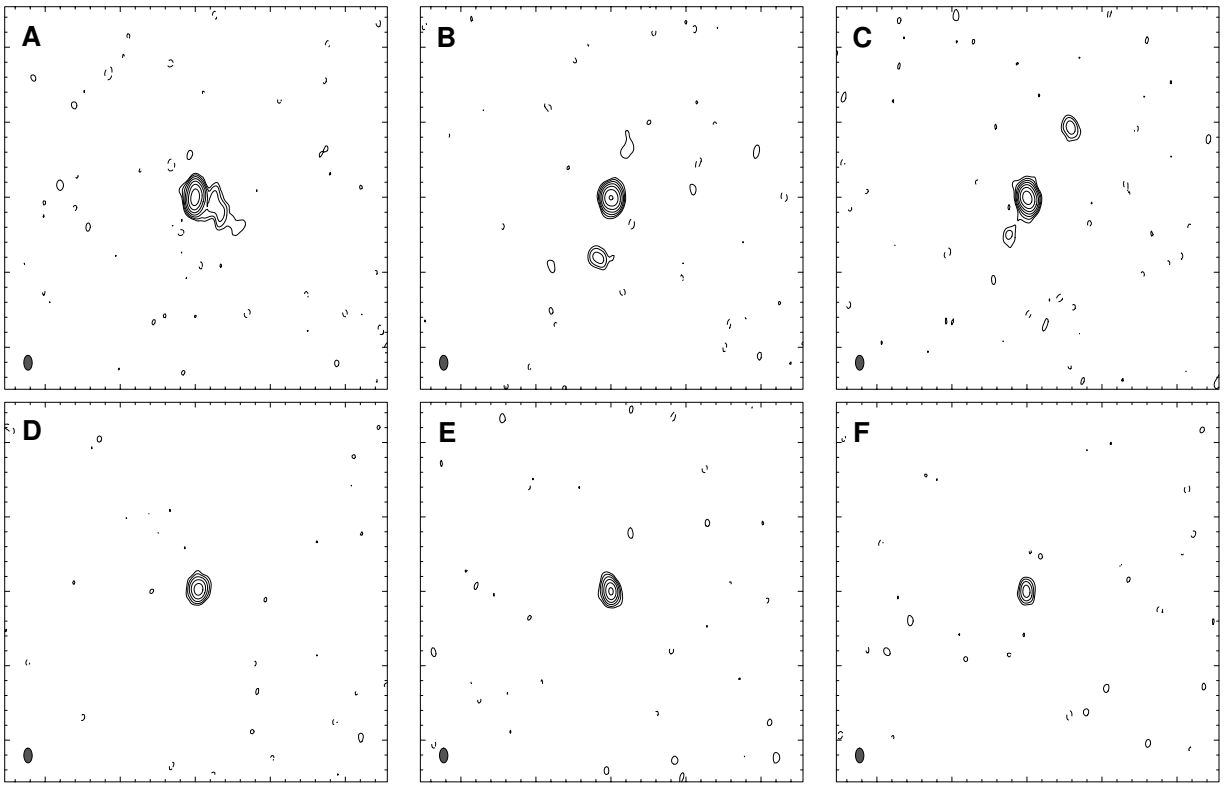

Fig. 2.— VLBA 1.7 GHz naturally-weighted maps of B1359+154 components. Top: A, B, C. Bottom: D, E, F. The beam is 9.88×5.54 mas at PA $= 1.11°$. Each box size is 250×250 mas. Contours are at $3, 6, 9...\times$ the map rms.

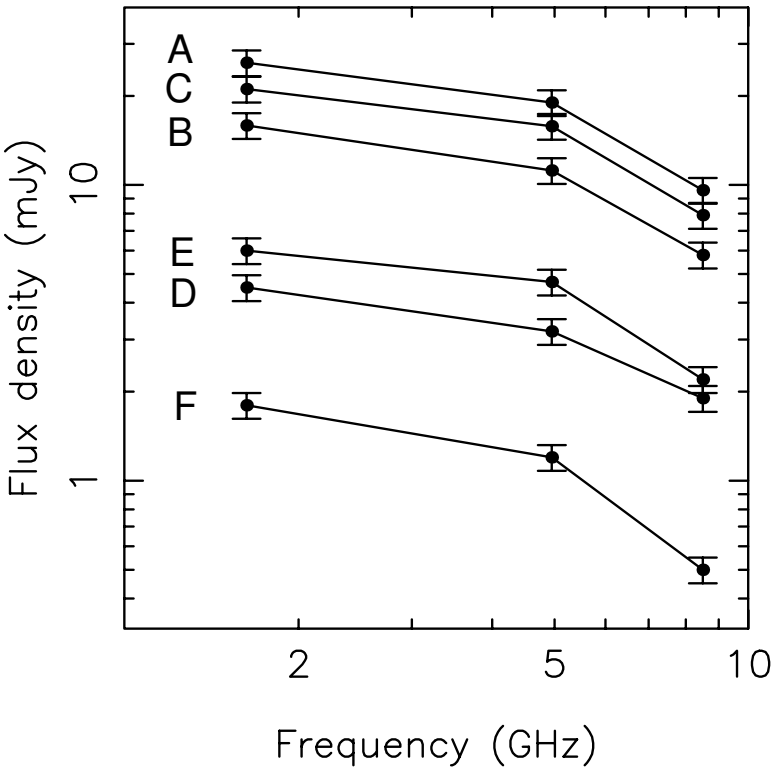

Fig. 3.— Radio spectra of B1359+154 components. Data from the 1.7 GHz VLBA, 5 GHz MERLIN (Rusin et al. 2000a) and 8.5 GHz VLA (Myers et al. 1999) observations. We assume flux density uncertainties of 5% to account for source variability and model-fitting errors.

the six components has a spectrum that is rather flat ($\alpha_{1.7}^{5} \simeq -0.3$, where $S_\nu \propto \nu^\alpha$) between 1.7 and 5 GHz, then falls off sharply ($\alpha_{8.5}^{15} \simeq -1.2$) between 5 and 8.5 GHz. The 1.7 – 5 GHz spectral indices for all six components (Table 1) agree within measurement errors. Even if the sharpness of the 5 GHz spectral break were somehow exacerbated by variability, it would still require that all six components vary in the same manner – something that would be impossible unless E and F are related to A–D. Therefore, the morphologies and low-frequency spectra of the B1359+154 radio components strongly suggest that they are six images of a single background source.

3. HST Imaging of B1359+154

Using the WFPC2 instrument on HST we obtained images of B1359+154 in the F555W ("V", 5200 sec) and F814W ("I", 5000 sec) bands on 2000 July 10. Each observation was divided into four subexposures, at two dither positions, which were used to remove cosmic rays and bad pixels. Fig. 4 shows the resulting images. Optical counterparts to all six radio components are observed, along with extended emission from the three galaxies. The images were modeled as a combination of point sources and de Vaucouleurs models following the modeling procedures of Lehár et al. (2000) for CASTLES observations of other lenses. Astrometric and photometric results are presented in Table 2. The positions of images A–F derived from the HST data match the radio positions to an accuracy of $0\farcs02$, consistent with our internal error estimates.

All six optical counterparts of the radio components are blue, with an average color of V–I= 0.5 mag and a dispersion in the colors of only 0.1 mag. The flux ratios of the 6 radio components and their optical counterparts differ by less than a factor of two between 1.7 GHz and the V-band, so they must be six lensed images. Three of the counterparts (A, B and C) are clearly extended in both the V and I-band images, consistent with the presence of an Einstein ring in the Rusin et al. (2000a) infrared image. The rest frame wavelengths of the V and I-band filters at the source redshift of $z_s = 3.235$ are 1300Å and 1900Å, respectively, so the host galaxy of the radio source must have a strong ultraviolet continuum to produce the arcs. While we lack images in bluer filters, and the Myers et al. (1999) spectrum of the source is contaminated by AGN activity, the host galaxy appears to be a star-forming Ly-break galaxy. The emission lines from the source are relatively narrow (Lyα and NV are well resolved) and lines characteristic of both AGN (CIV) and star formation (CIII]) are seen in the spectrum.

The optical counterparts (G, G′, G″) of the three infrared sources K1–K3 are extended and red. We have relabeled the sources using the standard CASTLES convention in which G is the most luminous lens and G′/G″ are of lower luminosity. All three are seen in the I-band image and essentially vanish in the V-band image, with a color of V–I$\gtrsim$ 3 mag. They are clearly three distinct galaxies which are well modeled by de Vaucouleurs profiles, rather than compact star-forming regions in a larger galaxy. With separations of only $4h^{-1}$ kpc (for $z_l \simeq 1.0$ in an $\Omega_0 = 0.3$ flat cosmological model), they are likely to be the core of a compact group. Unlike other lenses with secondary lens galaxies, the three galaxies have similar luminosities. Redshift estimates based on

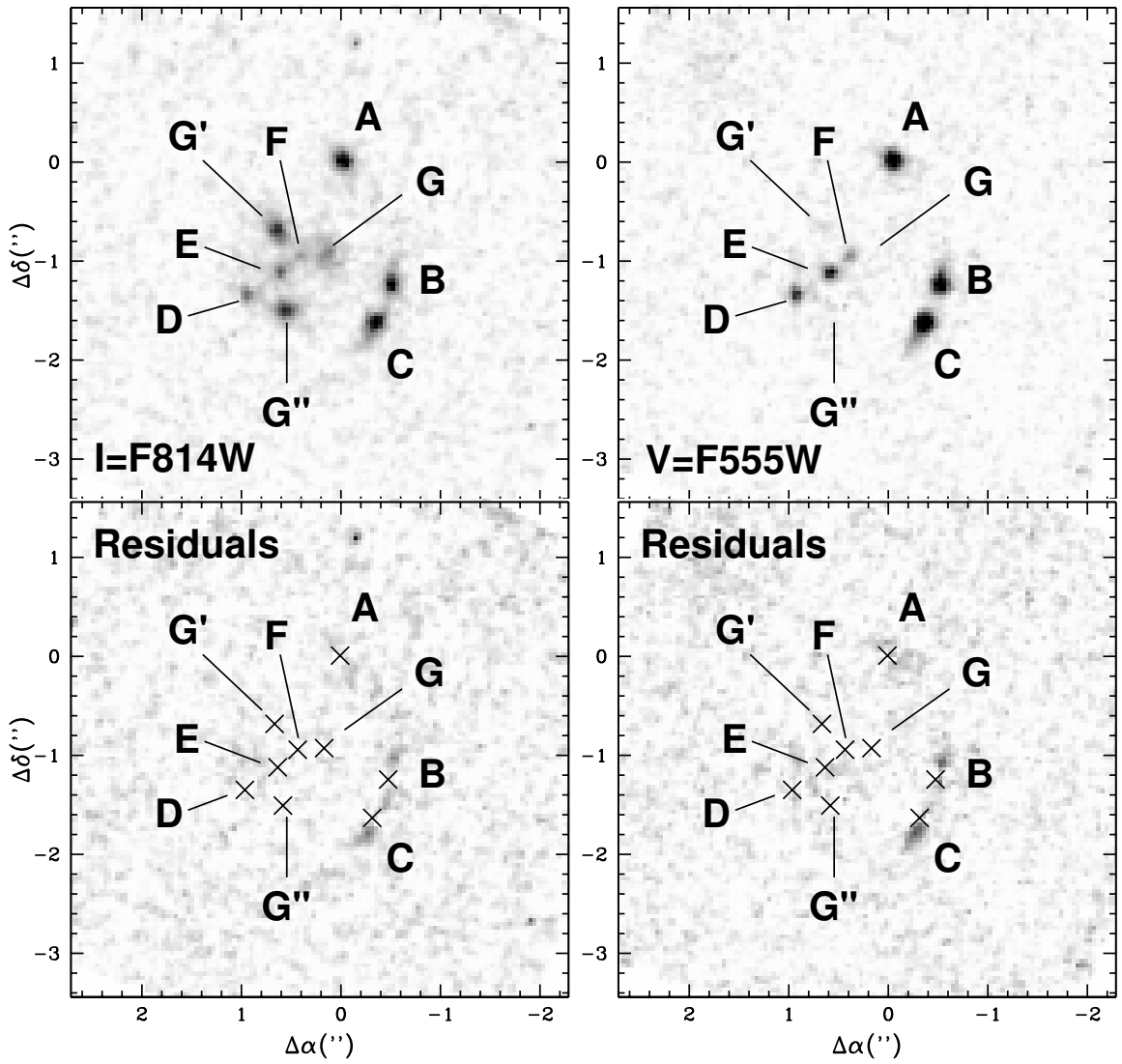

Fig. 4.— HST I-band (left) and V-band (right) images of B1359+154. The top panels show the final images with the components labeled as in Table 2. The bottom panels show the residuals after subtracting counterparts to the six radio cores and the three lens galaxies. Crosses mark the centers of the subtracted components.

their optical colors and the mass estimates derived from our models of the system (§4) and the fundamental plane (Kochanek et al. 2000a) are mutually consistent. We find $z_l = 1.35 \pm 0.16$, 0.88 ± 0.06 and 0.94 ± 0.07 for galaxies G, G′, and G″, respectively. The average redshift is $z_l = 1.05 \pm 0.20$ and the weighted average is $z_l = 0.94 \pm 0.04$, but for simplicity we will just assume $z_l = 1$ for future estimates. The scatter of the individual estimates is consistent with the scatter found by Kochanek et al. (2000a) for lenses with known redshifts. Such a group of galaxies is unlikely to be a projection effect given the separations and the size of the overall lens sample. Based on the results in the Appendix we estimate that the *a posteriori* probability of finding such a chance projection in a sample of 60 lenses is $\sim 10^{-3}$. We conclude that the lens is the core of a compact galaxy group (see Hickson 1997 for a review of compact groups). With three lens galaxies of comparable luminosity and redshift inside their joint Einstein ring, the gravitational potential should have additional extrema inside the triangle formed by the galaxies. While images A–D resemble a standard four-image lens morphology, two additional images (E and F) lie in the region between the three primary lenses. *Therefore, HST observations offer powerful evidence that B1359+154 is the first example of a true six-image galaxy-scale gravitational lens system.*

We also cataloged the nearby galaxies in the HST images using the SExtractor package (Bertin & Arnouts 1996). The software classified the optical objects, and computed total magnitudes using Kron-type automatic apertures (see Lehár et al. 2000). Colors were computed using fixed apertures scaled to the F814W size of each object. Table 3 lists all the galaxies detected by HST within $20''$ of the lens, after visually confirming the SExtractor classification. The galaxies were labeled G# in order of decreasing I-band brightness, or K# for the galaxies found in the Rusin et al. (2000a) infrared observations which were not detected in the I-band image. Table 3 also includes an estimate of the shear perturbation each neighboring galaxy can produce on the lens assuming they lie at the same redshift and have the same mass-to-light ratios (see Lehár et al. 2000). The sum of the shear contributions is $\gamma = 0.074$ at $\theta_\gamma = 83°$, although the largest source of shear, galaxy G1, is probably a foreground galaxy. The contribution of all the other galaxies is $\gamma = 0.049$ at $\theta_\gamma = -60°$.

4. Preliminary Mass Models

Constructing any believable model for the lensing mass of B1359+154 is a significant challenge. At a minimum the model must include mass distributions to represent each of the three lensing galaxies plus environmental contributions to the lensing potential, either in the form of external shear or a separate group halo. Since even the simplest models require a large number of free parameters, the best hope for producing a realistic mass model may ultimately rely on constraints from deep HST imaging of the extended arc emission (Kochanek, Keeton & McLeod 2000b). For now our primary objective is to demonstrate that a six-image lens system can be naturally produced by the observed lensing galaxies.

All models are constrained with 12 coordinates and 5 flux density ratios of the lensed radio

components, as derived from the VLBA data listed in Table 1. Only the core components A1–F1 are used at this time. We set a fit tolerance of 1 mas for the image positions and assume a 10% uncertainty on the flux densities. The galaxy positions are constrained according to the astrometric error bars given in Table 2. The goodness-of-fit parameter is therefore $\chi^2_{tot} = \chi^2_{pos} + \chi^2_{flx} + \chi^2_{gal}$, which includes contributions to the fit from the positions of the radio components, (χ^2_{pos}), their flux (χ^2_{flx}), and the positions of the lens galaxies (χ^2_{gal}). The redshift of the group is set at $z_l = 1$, and a flat cosmology with $\Omega_o = 0.3$ is assumed for all calculations. The models are optimized using the *lensmodel* software package (Keeton 2000).[9]

4.1. A Demonstration of Principle

Smooth gravitational potentials must produce an odd number of lensed images (Burke 1981). However, images can be trapped and demagnified in the singular or near-singular cores of lensing galaxies (Narasimha et al. 1986). We can label the possible image configurations by A/B, where A is the true number of images and B is the observed number of images. Since A is always odd, B1359+154 must be either a 7/6 or 9/6 system. A single lens can generate a 7/6 image configuration, but it should consist of 6 images near the Einstein radius of the system (see Keeton et al. 2000b). The central location of images E and F and the comparable luminosities of the three galaxies (1.0:0.4:0.4 for G:G′:G″) strongly suggest that all three lenses are important and that we are looking at a 9/6 lens system.

We begin by considering a compound mass distribution consisting of three singular isothermal spheres (SIS) in an external shear field. This model is unlikely to fit the data very well as it ignores galaxy ellipticity, but we use it to demonstrate the principles of compound deflectors in the context of B1359+154. From the expected caustic structure alone one can argue that 9/6 systems are possible. Each SIS deflector has an associated radial caustic on the source plane, at which an inward-crossing source produces a pair of images at the corresponding galaxy center: one observable and one trapped in the core. The asymmetry of the potential will also lead to at least one tangential caustic, at which an inward-crossing source produces a pair of observable images at the corresponding critical curve. Therefore, a 9/6 system is formed when a source sits within one tangential and three radial caustics. Because three positive parity images will be trapped in the galaxy cores, four of the observed images must have negative parity (saddle points in the time delay surface) to ensure that the parities of all nine images sum to 1 (Burke 1981; Blandford & Narayan 1986). Images A–D are arranged in a typical quad configuration, so we expect their parities to alternate in the usual way: A(+), B(–), C(+), D(–). This means that both E and F must correspond to saddle points (–), and we model the system under this assumption.

The critical curves, caustics and time delay surface for the best-fit 3SIS model are plotted in

[9]The code is publicly available at http://penedes.as.arizona.edu/ ckeeton/gravlens

Fig. 5. Because the separation of the galaxies is small compared to their Einstein radii, a single tangential critical curve encloses all three galaxies (Fig. 5a). This maps to the highly distorted tangential (astroid) caustic on the source plane (Fig. 5b). The large circular features in Fig. 5b correspond to the radial caustics associated with each SIS. These not only significantly overlap each other, but also overlap much of the astroid caustic creating a substantial 9/6 region in which the source resides. The cross-section of the model is dominated by 3/2, 5/3, 7/5 and 9/6 geometries, but it can also produce 7/4 and 11/8 configurations. The 11/8 region is due to the tangential caustic folding over on itself and creating a swallowtail catastrophe. The probability of observing 7/4, 7/5, 9/6 and 11/8 systems will be greatly enhanced through magnification bias. Despite the complexity of the caustic structure, the topology of the virtual time delay surface (Fig. 5c) is quite generic (Schneider 1985; Blandford & Narayan 1986). Images A–D have the standard topology for four-image lenses. Images A–C are associated with a *lemniscate* critical contour encompassing two minima (A and C) and the saddle point (B). Image D is a saddle point associated with a *limaçon* contour which would usually encompass images A–C in the large loop and the core of the lens galaxy in the smaller loop. In this case, however, the smaller loop contains all three lens galaxies. Images E and F lie at the saddle points of two new *lemniscate* critical contours with maximum-saddle-maximum topologies, where the maxima sit on the galaxy cores.

The 3SIS model has a best-fit of $\chi^2 = 1570$ for NDF = 10, and its parameters are listed in Table 4. The model poorly fits the positions of images A ($\chi^2_{pos,A} = 323$), B ($\chi^2_{pos,B} = 659$) and F ($\chi^2_{pos,F} = 299$). The flux density of image A is also significantly lower than observed (predicted 2.4 mJy, $\chi^2_{flx,A} = 80$). Given the simplicity of the model, the errors in the image positions are of little concern and should be greatly improved by adding ellipticity or adjusting the radial mass profiles of the galaxies. The mismatch of the flux densities is a more generic problem. Components B and C are clearly a merging pair of images associated with the tangential critical curve, and in most lens systems would be the brightest images. To reproduce the observed flux ordering in B1359+154, the critical curve must pass closer to A than either B or C, so that A will be the most magnified.[10] The 3SIS model is unable to accomplish this, as A sits quite far from the tangential critical curve (Fig. 5a). Accounting for the relative fluxes will therefore require models with more free parameters.

4.2. More Realistic Models

We now attempt to improve the fits to B1359+154 by investigating more realistic lens models. The mass distributions of lensing galaxies are ellipsoidal rather than spherical, so we consider models with 3 singular isothermal ellipsoids (SIE) in an external shear field. The SIE is described

[10]It is conceivable that the brightness of A may be produced by microlensing due to substructure in the lensing mass distribution (Schneider & Mao 1998). However, the large required amplification makes this less likely.

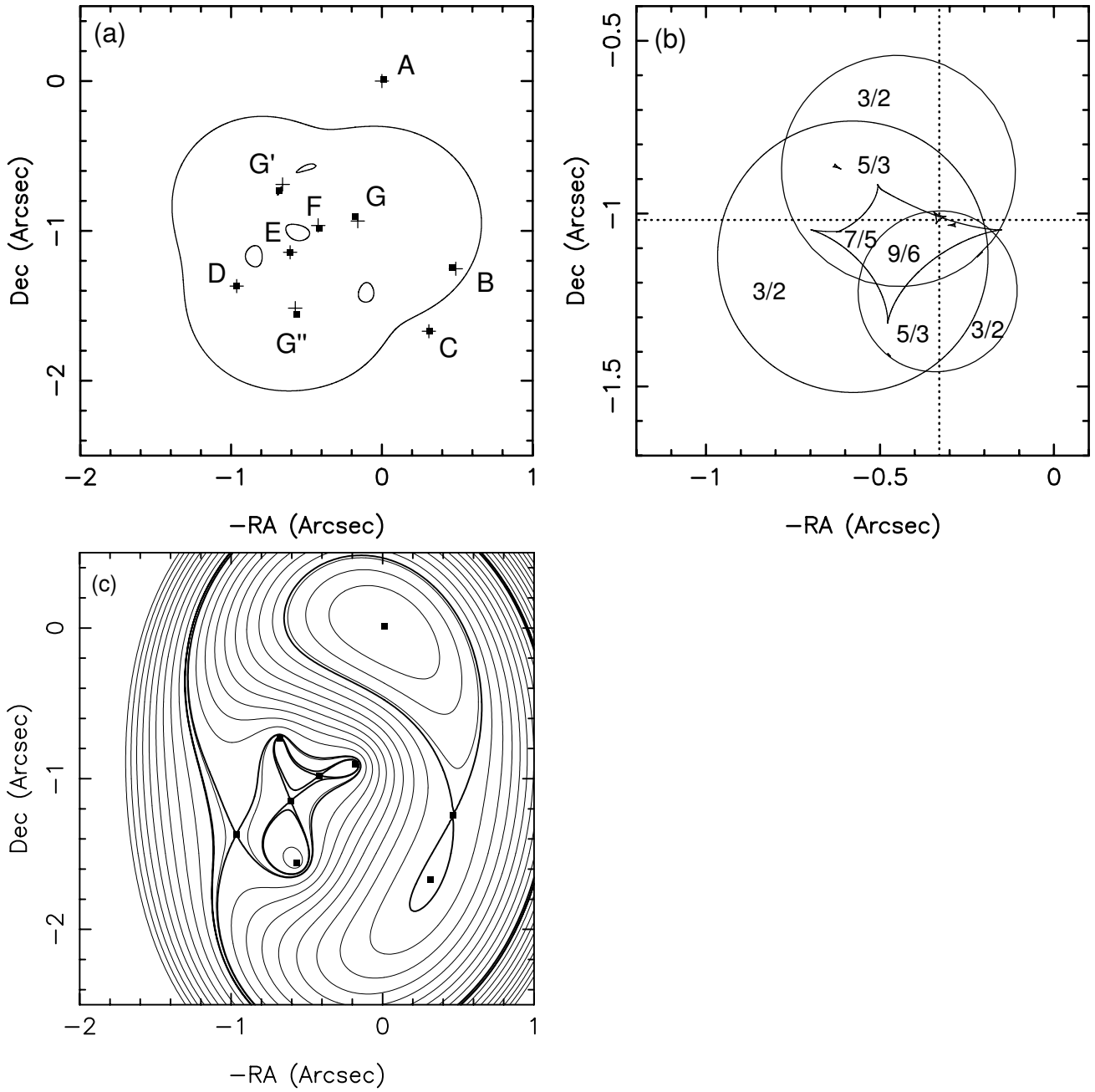

Fig. 5.— Best-fit 3SIS model. (a) Critical curves. Observed (model-predicted) image and galaxy positions are marked as crosses (squares). Note that A is far from the tangential critical curve, and thus cannot be highly magnified in this model. (b) Caustic curves. Prominent imaging regions are marked as A/B, where A is the total number of images and B is the observable number of images. The source sits at the intersection of the dotted lines, near a swallowtail catastrophe. (c) Contours of constant time delay, in steps of $3h^{-1}$ days outward from A (thin lines), except for the critical contours (bold lines) passing through the saddle points in this surface (B, D, E and F). Images trapped in the galaxy cores correspond to local maxima.

by the scaled surface mass density

$$\kappa(x,y) = \frac{b/2}{[(1-\epsilon)x^2 + (1+\epsilon)y^2]^{1/2}} \tag{1}$$

where b is the critical radius and $\epsilon = (1-f^2)/(1+f^2)$ is the ellipticity, with f as the mass axial ratio. In one set of trials we fix the orientations of G, G′ and G″ according to the de Vaucouleurs surface brightness profiles listed in Table 2. We refer to this as the 3SIE/FIX model. However, because these orientations are not very well constrained by HST, we also run trials in which the position angles of the galaxies are left as free parameters (3SIE model). Finally, we recognize that galaxies forming the core of a compact group may be truncated on the scale of the inter-galaxy separation. We thus consider pseudo-Jaffe (PJ) models (Keeton & Kochanek 1998), which have a truncation radius at which the density breaks from $\rho \propto 1/r^2$ to $1/r^4$. The PJ profile is described by

$$\kappa(x,y) = \frac{b/2}{[(1-\epsilon)x^2 + (1+\epsilon)y^2]^{1/2}} - \frac{b/2}{[(1-\epsilon)x^2 + (1+\epsilon)y^2 + a^2]^{1/2}} \tag{2}$$

We set $a = 0\farcs3$, roughly half the inter-galaxy separation in this system, and investigate models with spherical (3PJS) and elliptical (3PJE/FIX, 3PJE) pseudo-Jaffe deflectors.

The 3SIE/FIX model has a fit statistic of $\chi^2_{tot} = 216$ for NDF = 7, significantly improving upon the 3SIS model with regard to the image positions ($\chi^2_{pos} = 4$). The flux densities are still poorly matched to their observed values ($\chi^2_{flx} = 182$). The model-predicted flux densities of A–C are each much fainter than observed, and the fit to image A is particularly poor (predicted 2.8 mJy, $\chi^2_{flx,A} = 77$). It is unlikely that any fine-tuning of the model will remove this discrepancy so long as the galaxy position angles remain fixed.

The 3SIE model relaxes constraints on the galaxy orientations and provides the best fit of any model we investigate, $\chi^2_{tot} = 43$ for NDF = 4. The critical curves, caustics and time delay surface are plotted in Fig. 6. In this model the critical curve passes closer to A than either B or C (Fig. 6a), ensuring that A will be the brightest image. The key ingredient here is the placement of the unlensed source, which lies very close to the cusp of a swallowtail catastrophe inside the tangential caustic (Fig. 6b). As the source approaches this cusp, A diverges in magnification and would split into three adjacent images upon crossing into the 11/8 region. Therefore A can be highly magnified by placing a source just outside the swallowtail cusp. The largest contribution to the 3SIE fit statistic comes from the flux density of C (predicted 10.6 mJy, $\chi^2_{flx,C} = 22$). This is not a serious concern, as a slight shifting of the critical curve from B toward C could reproduce the proper flux ordering, and may be accomplished through unmodelable substructure in the lensing mass distribution. The second largest contribution is from the RA of galaxy G ($\chi^2_{gal,G} = 15.6$), which accounts for nearly all of $\chi^2_{gal} = 16.0$. This is exacerbated by the small estimated uncertainty ($0\farcs008$) of this coordinate. If we have underestimated the error, or had used circular error bars of radius equal to the major axis of the error ellipse ($0\farcs024$ for G), χ^2_{gal} would be much smaller ($\simeq 2$).

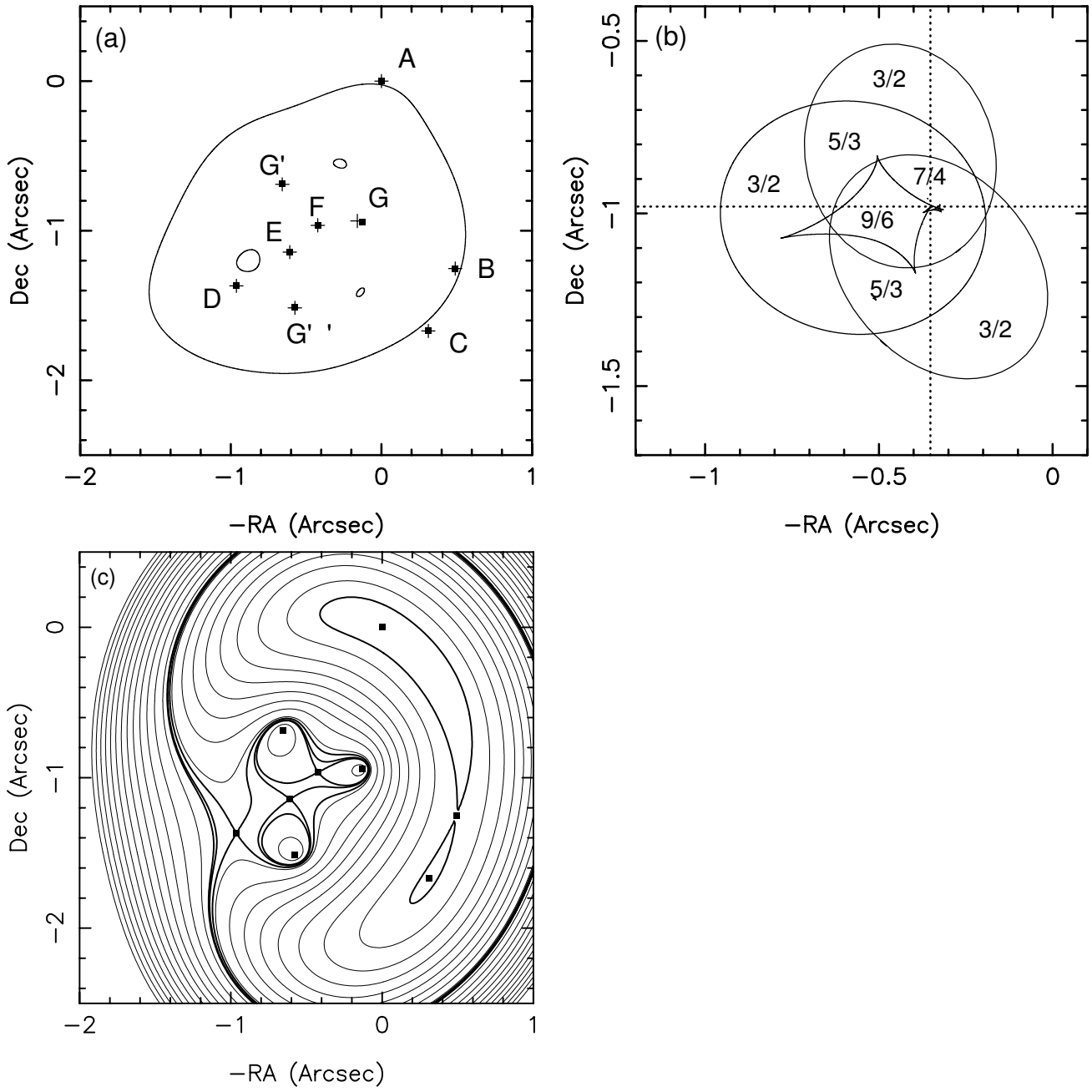

Fig. 6.— Best-fit 3SIE model. Plots are the same as in Fig. 5. Note that the critical curve (a) passes closer to A than either B or C, ensuring that A is the brightest image. The high magnification of A is due to the position of the unlensed source, which lies just outside a swallowtail cusp (b).

We now turn to the truncated mass distributions. The 3PJS model has a fit statistic of $\chi^2_{tot} = 538$, a significant improvement over the 3SIS model but with the same number of free parameters (NDF = 4). The flux density of A is 11.2 mJy compared to the observed value of 22.6 mJy, but overall the flux densities are fit rather well ($\chi^2_{flx} = 46$). The fit statistic is dominated by offsets from the galaxy positions ($\chi^2_{gal} = 290$). The 3PJE/FIX model also does better than its SIE counterpart, offering a fit of $\chi^2_{tot} = 100$ for NDF = 7. This is dominated by the fit to the flux density of A (predicted 8.8 mJy, $\chi^2_{flx,A} = 37$). The 3PJE model offers a best-fit of $\chi^2_{tot} = 65$, but again, A is not the brightest image (predicted 11.3 mJy, $\chi^2_{flx,A} = 25$). It is interesting to note that while the 3SIE model more accurately reproduces the flux density of A, the predicted galaxy position angles in the 3PJE model (69°, 18°, 62° for G, G′ and G″, respectively) are much closer to those of the observed surface brightness distributions (48°, 29°, 63°, respectively). However, the external shears in the 3PJE and 3PJE/FIX models ($\gamma \simeq 0.25$) are significantly larger than those in the 3SIE and 3SIE/FIX models ($\gamma \simeq 0.15$).

To test whether the large external shears predicted by each of our lens models may be due to a dark matter halo associated with the galaxy group, we also investigated models with four distinct mass distributions. The external shear was set to zero in these trials. Although one might expect the three primary lenses to define the group center, we were unable to find reasonable models in which the group halo resides within the Einstein ring. Problems arise because a fourth mass distribution that is even moderately concentrated significantly disturbs the caustic structure of the system, unless it is centered on one of the lensing galaxies. This makes it very difficult to account for the image properties without creating additional lensed components. Not surprisingly, we find that in the vast majority of our trials the group halo is pushed out of the Einstein ring toward the east, where it becomes a large external shear contributor.

We can check whether the mass ratios of the galaxies, as estimated from their lens model critical radii b, are consistent with the observed luminosity ratios. In standard lens models and observations of lenses, $b \propto L^{1/2}$ (see Keeton, Kochanek & Falco 1998), so we predict critical radius ratios of $1.0{:}0.62 \pm 0.2{:}0.63 \pm 0.2$ for G:G′:G″ based on the I-band luminosities in Table 2. The model ratios – 1.0:0.59:0.86 (3SIS), 1.0:0.62:0.75 (3SIE/FIX), 1.0:0.80:0.82 (3SIE), 1.0:0.85:0.55 (3PJS), 1.0:0.68:0.60 (3PJE/FIX), and 1.0:0.57:0.68 (3PJE) – are remarkably consistent with these predictions. This provides additional evidence that all three lensing galaxies are important to the model and indicates that the B-band (for $z_l \simeq 1$) mass-to-light ratios of the three lenses must be very similar. The compatible galaxy colors and the consistency of our fundamental plane redshift estimates further reinforce this argument.

5. Discussion

HST and VLBA observations demonstrate that the gravitational lens B1359+154 consists of six images of a single background radio source. This is the first example of a galaxy-scale lens system with more than four images. The unique configuration is produced by the complex

mass distribution of the lens, a compact group of three $z_l \simeq 1$ galaxies lying on the vertices of a triangle separated by $0\farcs7 \simeq 4h^{-1}$kpc, inside the $1\farcs7$ diameter Einstein ring defined by the radio components. The outer images (A–D) have the morphology of a standard four-image lens, but the triangle of galaxies produces additional extrema in the gravitational potential at which two central images (E and F) form. Simple lens models consisting of three deflectors constrained by HST galaxy coordinates and VLBA radio component data naturally produce six images at the observed positions, but require finely-tuned ellipticities to account for the flux density ratios. While it would be premature to claim that we have accurately represented the lensing mass distribution ($\chi^2_{tot}/\mathrm{NDF} \geq 10$ for all models), our initial modeling efforts demonstrate that B1359+154 can be explained as a true six-image lens system produced by three lensing galaxies. The consistency between the model-predicted deflector mass ratios and the observed luminosity ratios of the lens galaxies adds credibility to our results.

The three primary lens galaxies appear to constitute the core of a compact group. The most concentrated groups with small numbers of galaxies are the Hickson groups, a quarter of which have 3 members (Hickson et al. 1992). Separated by only $\simeq 4h^{-1}$ kpc, the three galaxies are close enough so that they might be expected to be consumed in a merger on a time scale of $\sim 0.1\ H_o^{-1}$ (Barnes 1985). Thus the incidence of high multiplicity arcsecond-scale lens systems may allow for an estimate of the merger rate of massive galaxies at $z \simeq 0.5 - 1.5$.

The relative simplicity of B1359+154 compared to the lenses found in the cores of rich clusters should make this system an excellent tool for studying galaxy halos in dense environments, and the relationship between the galaxies and their parent halos. One issue worthy of investigation is whether the galaxy mass distributions are truncated on the scale of inter-galaxy separation. The improved fits of the 3PJS and 3PJE/FIX models relative to the 3SIS and 3SIE/FIX models offer tentative arguments to this effect. Because predicted time delays in the PJ models are significantly higher than those in the SIE models, measured delays may be used to discriminate between the profiles. A second interesting issue is the placement of the group halo relative to the lensing galaxies. The image positions and flux densities can be reproduced by three mass distributions associated with the observed galaxies, so there is little need to add a fourth independent mass distribution inside the Einstein ring based on modeling arguments. A fourth deflector above the critical density for multiple imaging would place an additional radial caustic onto the source plane and disturb the delicate balance needed to account for the data without creating additional images. Thus if this halo exists within the Einstein ring, it is likely to be either subcritical (large core radius) or centered on one of the galaxies. However, the similar model-predicted mass-to-light ratios of the galaxies argue against the latter possibility. The large external shear fields ($\gamma \gtrsim 0.15$) required by all of our models suggests that a group halo may be displaced from the primary lenses. It is interesting to note that the orientation of the shear axis is remarkably constant, running nearly east to west regardless of the deflector model employed.

The six lensed components allow for more complicated models than we have investigated here, but the development of a truly robust model of the lensing mass distribution requires the

acquisition of additional constraints. The detection of lensed extended emission from the quasar host galaxy in both the HST optical and CFHT infrared images is particularly promising. Deep, high-resolution HST imaging using either WFPC2 or NICMOS could investigate the properties of the Einstein ring in detail and provide vital new constraints on the potential structure (see Kochanek et al. 2000b). Furthermore, if subcomponents of D, E and F can be detected using deep global VLBI imaging, the relative orientations of the radio substructure could place additional constraints on the local magnification matrices. Finally, the measurement of differential time delays would also offer important constraints on the mass model, as these directly probe the lensing potential at the image positions. One might expect the source to be variable, based on the compactness of the radio components, though there is no evidence for significant variability at this point. Radio snapshots of B1359+154 should be routinely obtained to determine whether the variability is large enough to undertake a monitoring program using current instruments. Otherwise, the enhanced VLA may be able to determine time delays from the component light curves even if the source variability is only at the few percent level.

It seems unlikely that the lens is a chance projection of three galaxies (an *a posteriori* probability of $\sim 10^{-3}$ in a sample of 60 lenses), and their statistically identical colors further argues against this possibility. While the Next Generation Space telescope could directly determine the redshifts of all three galaxies, current telescopes can only measure the average redshift of the lenses unless they have narrow emission lines that are not apparent in the Myers et al. (1999) spectrum. Two possibilities are to search for Mg II metal absorption lines in the source spectrum or HI absorption features in the radio continuum once the average redshift is known. For $z_l \simeq 1$ the Mg II absorption features would lie in the V-band where the source flux is 23 V mag, so the observation is difficult. Many groups have significant HI masses (Hickson 1997) and the radio flux density of $\simeq 90$ mJy at 0.7 GHz (based on the 1.7 GHz VLBA flux density and a spectral index of $\alpha \simeq 0.3$ at low frequency) may be high enough to search for absorption features. X-ray observations are less promising because very deep observations would be required to detect the group (a bright 10^{42} erg s^{-1} group at $z_l = 1$ has an X-ray flux of only 4×10^{-16} ergs cm^{-2} s^{-1}) and the high resolution of the Chandra Observatory would be needed to distinguish emission from the group and the lensed sources.

Acknowledgements: The authors deeply thank the director of STScI, Steve Beckwith, for making these observations possible. We also thank Lars Hernquist and Ann Zabludoff for discussions about groups and the implications of this lens. DR acknowledges support from the Zaccheus Daniel Foundation. Support for the CASTLES project was provided by NASA through grant numbers GO-8175, GO-8268 and GO-8804 from the Space Telescope Science Institute, which is operated by the Association of Universities for Research in Astronomy, Inc. CSK, EEF, JL, BAM and JAM were also supported by the Smithsonian Institution. CSK and CRK were also supported by the NASA Astrophysics Theory Program grant NAG5-4062. HWR is also supported by a Fellowship from the Alfred P. Sloan Foundation.

A. The Statistics of Perturbing Galaxies

Here we expand on the discussions of the statistics of perturbing galaxies of gravitational lenses in Keeton, Kochanek & Seljak (1997) and Kochanek & Apostolakis (1988) to include the effects of the galaxy luminosity function. We also emphasize the important distinction between a primary lens galaxy possessing a nearby neighbor and that neighbor significantly perturbing either the lens model or the caustic structure. We consider only galaxies which are clustered with the primary lens galaxy. Galaxies and clusters along the line of sight are an important source of weak shear perturbations but clustered galaxies dominate the perturbations (see Keeton et al. 1997; Barkana 1996). A key distinction to bear in mind is that *all* lens galaxies will have close neighbors (or satellites) if examined closely, so it is only the degree to which they modify the caustic structure or perturb the images of the lens which is relevant. Moreover, the $0.1-1\%$ astrometric precision of most lens observations permits the detection of very small perturbations to lens models unless they are degenerate with other properties of the mass model. The sensitivity of models to small perturbations means that neighbors may be important to all lens models while remaining unimportant for most statistical properties of lens systems (image separations, image multiplicities, cross sections, etc.).[11]

Following Keeton et al. (1997) and Kochanek & Apostolakis (1988) we model the distribution of neighbors using the correlation function, $\xi(r)=(r/r_0)^{-\chi}$ with $r_0\simeq 5h^{-1}$ Mpc and $\chi\simeq 1.75$ (e.g. Peebles 1993), which when projected onto the lens plane becomes $\xi_2(R)\simeq 4r_0^{\chi}R^{1-\chi}$. We assume that the correlation function can be extrapolated to the small physical scales relevant to the calculations. We will add the effects of the distribution of galaxies in luminosity by including a luminosity function, $dn/dL=n_*(L/L_*)^{\alpha}\exp(-L/L_*)$ where $n_*\simeq 0.01(h\mathrm{Mpc})^{-3}$ and $\alpha\simeq -1$ (e.g. Kochanek 1996). We use an SIS lens model to estimate the critical radius $b=b_*(L/L_*)^{1/2}D_{LS}/D_{OS}$ and the Faber-Jackson relation to convert between luminosity and velocity dispersion, $L/L_*=(\sigma/\sigma_*)^4$. D_{OL}, D_{OS} and D_{LS} are standard angular diameter distances and $b_*=4\pi(\sigma_*/c)^2=1\farcs45$ for early-type lens galaxies (Kochanek et al. 2000a). The characteristic scale for finding neighboring galaxies is given by the probability of finding a galaxy with a comoving density n_* inside the critical radius b_* of an L_* lens galaxy,

$$\tau_0 = 2\pi n_*\int_0^{b_*D_{OL}} RdR\xi_2(R)\simeq 20n_*r_0^{\chi}(b_*D_{OL})^{3-\chi} \tag{A1}$$

$$\simeq 0.005\left[\frac{n_*}{0.01(h\mathrm{Mpc})^{-3}}\right]\left[\frac{r_0}{5h^{-1}\mathrm{Mpc}}\right]^{1.75}\left[\frac{b_*D_{OL}}{5h^{-1}\mathrm{kpc}}\right]^{1.25}. \tag{A2}$$

[11] We will discuss only pairs of galaxies. While the probability of three galaxies can be determined from the three-point correlation function, it has never been measured on the kpc scales corresponding to the separations of galaxies in compact groups. An empirical determination based on a local redshift survey would probably be the most accurate approach to making the estimate.

The probability of finding a galaxy brighter than luminosity L is

$$\tau(>L) = \tau_0 \int_{L/L_*}^{\infty} d\lambda \exp(-\lambda)\lambda^{\alpha} \tag{A3}$$

where $\lambda = L/L_*$. The integral logarithmically diverges as $L \to 0$ for $\alpha = -1$, but the divergence is slow, as the integral is 0.2, 1.8 and 4.0 for $L/L_* = 1$, 0.1 and 0.01, respectively. The result (A3) is an underestimate for several reasons. First, early-type galaxies are more strongly clustered than galaxies in general, so our value of r_0 is low. Second, for detecting neighbors we should include both early-type and late-type galaxies, and the total density of all types of galaxies is larger than $0.01(h^{-1}\mathrm{Mpc})^{-3}$.

The third problem is that the presence of multiple galaxies modifies the cross sections for finding the system as a gravitational lens. Kochanek & Apostolakis (1988) showed that for galaxies with equal critical radii b_0 separated by distance ℓ, the total cross-section is approximately $2\pi b_0^2$ for $\ell > 4b_0$, $\pi b_0^2\,[2-(2-l/2b_0)]^2$ for $2b_0 < \ell < 4b_0$ and $\pi(2b_0 - \ell/2)^2$ for $\ell < 2b_0$. The cross-section has a *minimum* at $\ell = 2b_0$ where the centers of the two lenses are deflected to the same point on the source plane. Where the total cross-section is smallest, the cross-section for more than two images and the average image magnification are largest. In short, as the cross-section is dropping, the amount of magnification bias will rise in compensation. For two galaxies with critical radii b_1 and b_2 separated by ℓ we can derive several general results. There are no critical lines on the axis separating the two galaxies once $\ell < (b_1^{1/2} + b_2^{1/2})^2$, while the lens can generate images bracketing both lenses once $\ell < 2(b_1 + b_2)$. If the separation is smaller than $\ell < 2\max(b_1, b_2)$ then it is possible to find solutions with no images in between the two lenses. Kochanek et al. (2000b) used this to find a model for the four-image lens B1608+656 using two singular galaxies. The total multiple image cross-section is $\pi(b_1^2 + b_2^2)$ when the lenses are well separated, rising to $\pi(b_1 + b_2)^2$ when they are perfectly aligned. The dependence of the cross section on separation should be similar to the equal critical radius case, with a minimum total cross-section and a maximum large image multiplicity cross-section at an intermediate separation $\ell \simeq (b_1 + b_2)$. Because $b \propto L^{1/2}$, relatively low luminosity galaxies can produce substantial cross-section enhancements – a L_* and $0.1L_*$ galaxy have a cross-section when aligned which is 60% higher than that for the two galaxies separately. We can estimate the magnitude of the effect by computing the fractional "excess" cross-section $2\pi b_1 b_2/\pi b_1^2$ for aligned lenses over well separated lenses, assuming that it holds for all lenses separated by less than $\ell < 2(b_1 + b_2)$. Defining $u = b_1/b_*$ the fractional excess cross-section from less massive neighboring galaxies ($b_2 < b_1$) is of order

$$\simeq 2^{4-\chi}\tau_0 \int_0^{u^2} d\lambda\lambda^{\alpha+1/2} \exp(-\lambda)(u + \lambda^{1/2})^{3-\chi}/u. \tag{A4}$$

For $u = 1$ ($b_1 = b_*$) the excess cross-section is $11\tau_0 \sim 6\%$, while for $u = 0.1$ it is only $0.9\tau_0$. While a numerical calculation including the effects of magnification bias is needed to obtain the exact impact of neighbors on lensing statistics, this order of magnitude calculation shows that the enhancements are modest.

Keeton et al. (1997) considered a very simple model for the importance of neighboring galaxies by estimating the shear that a companion can produce at the center of the primary lens galaxy. A neighbor of luminosity L located at projected radius R produces a shear $\gamma = (b_* D_{OL}/2R)(L/L_*)^{1/2}$ at the center of the primary lens. The probability of finding a shear larger than γ is

$$\tau(>\gamma) \simeq 0.4\tau_0\gamma^{-1.25}\int_0^\infty d\lambda\lambda^{\alpha+(3-\chi)/2}\exp(-\lambda) \tag{A5}$$

where $\lambda = L/L_*$. The integral converges (for standard parameters $\alpha + (3-\chi)/2 \simeq -0.38$ and the value of the integral is 1.4), and the perturbations are weakly dominated by low luminosity galaxies. While the probability of a lens having a neighbor diverges, the probability that the neighbor produces a large perturbation on the lens is finite and relatively small, $\tau(>\gamma) \simeq 0.6\tau_0/\gamma^{1.25}$. This estimate of the perturbations makes little sense for perturbing galaxies inside the Einstein ring or for estimating the perturbations to images at the Einstein radius. If we instead estimate the shear produced at the closest point on the unperturbed critical line of radius b_0 of the primary lens, we find

$$\tau(>\gamma) \simeq \tau_0\left(\frac{b_0}{b_*}\right)^{1.25}\int_0^\infty d\lambda\lambda^\alpha\exp(-\lambda)\left|1-\left(1\pm\frac{b_*\lambda^{1/2}}{2\gamma b_0}\right)^{1.25}\right| \tag{A6}$$

where the + (−) branch corresponds to perturbations from outside (inside) the ring. The integral is not analytic, but under the approximation that $|1-(1\pm x)^a| = x^a$ we obtain the same result as in A3. The Keeton et al. (1997) approximation underestimates the total perturbation by about a factor of 2. The new approximation still overestimates the contribution from images inside the Einstein ring, because a perturbing galaxy located at the center is counted as producing a shear perturbation at the Einstein ring when its effects are indistinguishable from the monopole of the primary lens.

REFERENCES

Barkana, R. 1996, ApJ, 468, 17

Barnes, J. 1985, MNRAS, 215, 517

Benitez, N., Broadhurst, T., Rosati, P., Courbin, F., Squires, G., Lidman, C., & Magain, P. 1999, ApJ, 527, 31

Bertin, E., & Arnouts, S. 1996, A&AS, 117, 393

Blandford, R.D. & Kochanek, C.S. 1987, ApJ, 321, 658

Blandford, R.D. & Narayan, R. 1986, ApJ, 310, 568

Burke, W.L. 1981, ApJ, 244, L1

Chen, G.H., & Hewitt, J.N. 1993, AJ, 106, 1719

Colley, W.N., Tyson, J.A., & Turner, E.L. 1996, ApJ, 461, 83L

Dressler, A. 1980, ApJ, 236, 351

Fassnacht, C.D., et al. 1999, AJ, 117, 658

Fischer, P., Bernstein, G., Rhee, G., & Tyson, J.A. 1997, AJ, 113, 521

Garrett, M.A., Porcas, R.W., Nair, S., & Patnaik, A.R. 1996, MNRAS, 279L, 7

Hickson, P. 1997, ARA&A, 35, 357

Hickson, P., Mendes de Oliveira, C., Huchra, J.P., & Palumbo, G.G. 1992, ApJ, 399, 353

Ibata, R.A., Lewis, G.F., Irwin, M.J., Lehár, J., & Totten, E.J. 1999, AJ, 118, 1922

Kassiola, A., Kovner, I., & Fort, B. 1992, ApJ, 400, 41

Keeton, C.R. 2000, ApJ, submitted

Keeton, C.R., Christlein, D., & Zabludoff, A.I. 2000a, ApJ, in press (astro-ph/0007288)

Keeton, C.R., & Kochanek, C.S. 1998, ApJ, 495, 157

Keeton, C.R., Kochanek, C.S., & Falco, E.E. 1998, ApJ, 509, 561

Keeton, C.R., Kochanek, C.S., & Seljak, U. 1997, ApJ, 482, 604

Keeton, C.R., Mao, S., & Witt, H.J. 2000b, ApJ, 537, 697

King, L.J., Browne, I.W.A., Muxlow, T.W.B., Narasimha, D., Patnaik, A.R., Porcas, R.W., & Wilkinson, P.N. 1997, MNRAS, 289, 450

Kochanek, C.S. 1996, ApJ, 466, 638

Kochanek, C.S., & Apostolakis, J. 1988, MNRAS, 235, 1073

Kochanek, C.S., et al. 2000a, ApJ, 543, 131

Kochanek, C.S., Keeton, C.R., & McLeod, B.A. 2000b, ApJ, submitted (astro-ph/0006116)

Koopmans, L.V.E., et al. 2000, A&A, 361, 815

Koopmans, L.V.E., et al. 1999, MNRAS, 303, 727

Koopmans, L.V.E., & Fassnacht, C.D. 1999, ApJ, 527, 513

Lawrence, C.R., Schneider, D.P., Schmidt, M., Bennett, C.L., Hewitt, J.N., Burke, B.F., Turner, E.L., & Gunn, J.E. 1984, Science, 223, 46

Lehár, et al. 2000, ApJ, 536, 584

Mao, S., & Schneider, P. 1998, MNRAS, 295, 587

Meneghetti, M., Bolzonella, M., Bartelmann, M., Moscardini, L., & Tormen, G. 2000, MNRAS, 314, 338

Muñoz, J.A., et al. 2000, ApJ, submitted (astro-ph/0008124)

Myers, S.T., et al. 1995, ApJ, 447L, 5

Myers, S.T., et al. 1999, AJ, 117, 2565

Nair, S., & Garrett, M.A. 1997, MNRAS, 284, 58

Narasimha, D., Subramanian, K., & Chitre, S.M. 1986, Nature, 321, 45

Natarajan, P., Kneib, J.-P., Smail, I., & Ellis, R.S. 1998, ApJ, 499, 600

Peebles, P.J.E. 1993, Principles of Physical Cosmology (Princeton: Princeton Univ. Press)

Rusin, D., Hall, P.B., Nichol, R.C., Marlow, D.R., Richards, A.M.S., & Myers, S.T. 2000a, ApJ, 533L, 89

Rusin, D., & Ma, C.-P. 2000, ApJL, submitted (astro-ph/0009079)

Rusin, D., et al. 2000b, AJ, submitted

Schechter, P.L., et al. 1997, ApJ, 475L, 85

Schechter, P.L., & Moore, C.B. 1993, AJ, 105, 1

Schneider, P. 1985, A&A, 143, 413

Sykes, C.M., et al. 1998, MNRAS, 301, 310

Tyson, J.A., Kochanski, G.P., & Dell'Antonio, I.P. 1998, ApJ, 498L, 107

Wallington, S., Kochanek, C.S., & Koo, D.C. 1995, ApJ, 441, 58

Xanthopoulos, E., et al. 1998, MNRAS, 300, 649

Table 1. VLBA Data

Comp	ΔRA ($''$)	ΔDec ($''$)	$S_{1.7}$ (mJy)	b_{maj} (mas)	$\alpha^5_{1.7}$
A1	$\equiv 0$	$\equiv 0$	22.6	9	-0.29
B1	-0.490398 ± 0.00003	-1.252428 ± 0.00003	14.5	6	-0.32
C1	-0.311420 ± 0.00002	-1.669560 ± 0.00002	19.8	6	-0.27
D1	$+0.962772 \pm 0.00010$	-1.368612 ± 0.00010	4.5	5	-0.32
E1	$+0.608880 \pm 0.00008$	-1.142871 ± 0.00008	6.0	3	-0.23
F1	$+0.422273 \pm 0.00025$	-0.963759 ± 0.00025	1.8	3	-0.38
A2	-0.013783 ± 0.00013	-0.006793 ± 0.00013	3.3	16	
B2	-0.481571 ± 0.00032	-1.292351 ± 0.00032	1.4	8	
C2	-0.340726 ± 0.00034	-1.622677 ± 0.00034	1.3	7	

Note. — Model-fit components for B1359+154 1.7 GHz VLBA data (combined epochs). Positions are offset from RA $14^h\ 01^m\ 35^s.5476$, Dec $+15'\ 13''\ 25\overset{''}{.}646$ (J2000). Nominal uncertainties on the flux densities are three times the map rms of 45 μJy/beam. Positional uncertainties are taken as the beam size ($\sim$ 10 mas) divided by the signal-to-noise for each component. The major axes of the gaussian components are given by b_{maj}. Spectral indices $\alpha^5_{1.7}$ between 1.7 and 5 GHz are calculated using the combined flux density of the primary and subcomponents, where applicable. The 5 GHz data is from Rusin et al. (2000a). Assuming 5% errors on both the 1.7 and 5 GHz flux densities due to variability and model-fitting, the error on the spectral indices is $\simeq 0.07$.

Table 2. HST Astrometry and Photometry

ID	ΔRA (″)	ΔDec (″)	I (mag)	V–I (mag)	R_e (″)	e	PA (°)
A	≡0	≡0	24.01 ± 0.06	0.68 ± 0.12			
B	–0.483±0.007	–1.253±0.009	24.29 ± 0.11	0.43 ± 0.15			
C	–0.323±0.007	–1.640±0.003	24.01 ± 0.05	0.27 ± 0.13			
D	0.957±0.008	–1.357±0.008	25.19 ± 0.08	0.61 ± 0.17			
E	0.627±0.013	–1.129±0.011	25.12 ± 0.17	0.45 ± 0.19			
F	0.426±0.017	–0.951±0.028	26.25 ± 0.23	0.29 ± 0.23			
G	0.160±0.008	–0.935±0.024	22.68 ± 0.28	3.31 ± 0.55	0.71±0.29	0.11±0.23	48±55
G′	0.658±0.005	–0.690±0.008	23.69 ± 0.24	3.13 ± 0.29	0.16±0.06	0.69±0.14	29±8
G″	0.575±0.007	–1.516±0.011	23.70 ± 0.33	3.23 ± 1.01	0.14±0.07	0.49±0.20	63±7

Note. — The three lensing galaxies are fit to de Vaucouleurs profiles. The effective radii (R_e), ellipticity parameters $e = 1 - f$ and position angles (PA) of these fits are listed.

Table 3. Nearby Objects

ID	ΔRA (″)	ΔDec (″)	I	V–I	I–K	γ	θ_γ	Notes
G	0.2	–0.9	22.68 ± 0.55	3.31 ± 0.97	∼2.0			K3, Group
G′	0.7	–0.7	23.69 ± 0.14	3.13 ± 0.35	∼3.0			K1, Group
G″	0.6	–1.5	23.70 ± 0.12	3.23 ± 1.03	∼3.0			K2, Group
S1	4.4	9.3	24.39 ± 0.11	> 1.74				
S2	11.5	–2.9	24.94 ± 0.12	> 1.43				
G1	–13.5	–7.5	19.08 ± 0.10	1.36 ± 0.03		0.076	64	
G2	–16.8	1.7	22.73 ± 0.10	1.42 ± 0.05		0.013	–81	
G3	0.6	–10.6	23.30 ± 0.10	0.79 ± 0.04		0.017	–3	
G4	2.1	5.2	23.52 ± 0.11	0.94 ± 0.06		0.023	18	
G5	3.7	–1.3	23.52 ± 0.11	> 2.41	∼4.4	0.042	–85	K4, Group
G6	–17.5	6.7	23.58 ± 0.11	1.09 ± 0.06		0.008	–67	
G7	–9.1	–5.1	23.97 ± 0.11	1.17 ± 0.06		0.012	66	
G8	–7.1	8.4	24.31 ± 0.11	1.48 ± 0.08		0.009	–38	
G9	–1.8	1.5	24.50 ± 0.12	> 1.37	∼3.5	0.030	–38	K5, Group
G10	6.8	–12.2	24.70 ± 0.12	0.63 ± 0.09		0.007	–31	
G11	12.2	–2.6	24.80 ± 0.12	1.54 ± 0.09		0.007	–82	
K6	–6.5	–6.9	> 25.0		>4			K6
T1	–32.3	–67.8	18.26 ± 0.10	1.38 ± 0.03		0.023	26	
T2	–47.0	–9.9	18.85 ± 0.10	2.20 ± 0.03		0.027	79	
T3	–34.0	–50.1	19.23 ± 0.10	2.12 ± 0.03		0.018	35	

Note. — SExtractor position offsets from A are given in arcseconds. G,G′,G″ photometry and positions are from component fits in Table 2. Galaxies on the WFPC2 image within 20″ of G are labeled Gx, and those detected only in the Rusin et al. (2000a) infrared observations are labeled Kx. Stars are labeled as Sx. Galaxies outside of 20″ with large estimated shears are included as Tx. Tidal shear estimates γ assume SIS halos with the same redshift and mass-to-light ratio as G, and the shear position angles θ_γ are relative to G in degrees counter-clockwise from North (see Lehár et al. 2000).

Table 4. Lens Models

Type	Lens	b ($''$)	x_l ($''$)	y_l ($''$)	e, γ	PA ($^\circ$)	Img	Δt_{iA} (h^{-1}days)	χ^2
3SIS	G	0.400	0.179	−0.906	0.000	0.0	B	9.7	$\chi^2_{tot} = 1569.8$
	G′	0.236	0.680	−0.734	0.000	0.0	C	9.3	$\chi^2_{pnt} = 1341.6$
	G″	0.344	0.567	−1.559	0.000	0.0	D	35.8	$\chi^2_{flx} = 154.6$
	shear				0.154	87.9	E	36.8	$\chi^2_{gal} = 73.6$
	src		0.330	−1.018			F	36.9	
3SIE/FIX	G	0.409	0.135	−0.912	0.170	48.0	B	9.6	$\chi^2_{tot} = 215.8$
	G′	0.253	0.670	−0.718	0.000	29.0	C	9.2	$\chi^2_{pnt} = 3.9$
	G″	0.306	0.581	−1.506	0.139	63.0	D	33.0	$\chi^2_{flx} = 181.6$
	shear				0.123	97.4	E	34.0	$\chi^2_{gal} = 30.3$
	src		0.328	−0.991			F	34.3	
3SIE	G	0.359	0.128	−0.944	0.338	−10.6	B	1.0	$\chi^2_{tot} = 43.2$
	G′	0.287	0.658	−0.688	0.589	−47.6	C	0.8	$\chi^2_{pnt} = 0.2$
	G″	0.294	0.576	−1.513	0.416	−78.1	D	24.7	$\chi^2_{flx} = 27.0$
	shear				0.132	71.5	E	25.3	$\chi^2_{gal} = 16.0$
	src		0.352	−0.980			F	25.5	
3PJS	G	1.371	0.127	−1.030	0.000	0.0	B	17.6	$\chi^2_{tot} = 537.9$
	G′	1.170	0.618	−0.693	0.000	0.0	C	16.6	$\chi^2_{pnt} = 202.1$
	G″	0.754	0.649	−1.416	0.000	0.0	D	66.5	$\chi^2_{flx} = 45.8$
	shear				0.235	96.2	E	69.3	$\chi^2_{gal} = 290.0$
	src		0.223	−0.919			F	71.2	
3PJE/FIX	G	1.348	0.109	−0.964	0.171	48.0	B	20.5	$\chi^2_{tot} = 99.8$
	G′	0.914	0.664	−0.700	0.448	29.0	C	19.7	$\chi^2_{pnt} = 3.9$
	G″	0.812	0.581	−1.488	0.506	63.0	D	66.1	$\chi^2_{flx} = 44.0$
	shear				0.255	94.0	E	66.7	$\chi^2_{gal} = 51.9$
	src		0.242	−0.941			F	68.2	
3PJE	G	1.095	0.134	−0.962	0.581	69.2	B	27.5	$\chi^2_{tot} = 64.7$
	G′	0.626	0.658	−0.693	0.665	18.4	C	25.8	$\chi^2_{pnt} = 1.1$
	G″	0.745	0.580	−1.489	0.603	62.0	D	73.9	$\chi^2_{flx} = 45.1$
	shear				0.262	95.8	E	73.6	$\chi^2_{gal} = 18.5$
	src		0.230	−0.929			F	74.9	

Note. — The five lines for each model give the properties of the lensing galaxies (G, G′ and G″), external shear, and recovered source coordinates: b is the critical radius, x_l and y_l are the lens coordinates, $e = 1 - f$ where f is the axis ratio of the ellipsoid, γ is the strength of the external shear, and PA is the major axis position angle of the ellipsoid or the direction (to a tidal perturbation) producing the shear. The time delays for each image are defined relative to image A as $\Delta t_{iA} = t_i - t_A$ and were computed for an $\Omega_0 = 0.3$ flat universe and a lens redshift $z_l = 1$. The final column gives χ^2_{tot} and the contributions from the astrometry of the images (χ^2_{pos}), the flux ratios of the images (χ^2_{flx}) and the positions of the lens galaxies (χ^2_{gal}). The models assume that the uncertainties in the positions of the radio sources are 1 mas and that the fractional uncertainties in their flux densities are 10%.